Electrically controlled modulation in a photonic crystal nanocavity

Dirk Englund[1,2]**, Bryan Ellis**[1]**, Elizabeth Edwards**[1]**, Tomas Sarmiento**[1]**,**
James S. Harris[1]**, David A. B. Miller**[1] **and Jelena Vučković**[1]

[1]*Department of Electrical Engineering, Stanford University, Stanford CA 94305*
[2]*present address: Department of Physics, Harvard University, Cambridge MA 02138*

Abstract: We describe a compact modulator based on a photonic crystal nanocavity whose resonance is electrically controlled through an integrated p-i-n junction. The sub-micron size of the nanocavity promises very low capacitance, high bandwidth, and efficient on-chip integration in optical interconnects.

© 2009 Optical Society of America

OCIS codes: (130.3120) Integrated optics devices; (270.5580) Quantum electrodynamics; (230.5750) Resonators; (230.6080) Sources; (250.4110) Modulators.

References and links

1. D. A. B. Miller, "Device Requirements for Optical Interconnects to Silicon Chips," Proc. IEEE **97**, 1166 – 1185 (2009).
2. J. Meindl, "Interconnect opportunities for gigascale integration," Micro. IEEE **23**(3), 28–35 (2003).
3. M. Lipson, "Guiding, modulating, and emitting light on Silicon-challenges and opportunities," J. Lightwave Technol. **23**(12), 4222–4238 (2005).
4. J. D. Joannopoulos, S. G. Johnson, J. N. Winn, and R. D. Meade, *Photonic crystals: molding the flow of light*, 2nd ed. (Princeton University Press, Princeton, NJ, 2008).
5. H. Takano, B.-S. Song, T. Asano, and S. Noda, "Highly efficient multi-channel drop filter in a two-dimensional hetero photonic crystal," Opt. Express **14**(8), 3491–3496 (2006).
6. T. Matsumoto, T. Asatsuma, and T. Baba, "Experimental demonstration of a wavelength demultiplexer based on negative-refractive photonic-crystal components," Appl. Phys. Lett. **91**(9), 091117 (pages 3) (2007).
7. N. Hitoshi, Y. Sugimoto, K. Kanamoto, N. Ikeda, Y. Tanaka, Y. Nakamura, S. Ohkouchi, Y. Watanabe, K. Inoue, H. Ishikawa, and K. Asakawa, "Ultra-fast photonic crystal/quantum dot all-optical switch for future photonic networks," Opt. Express **12**, 6606–6614 (2004).
8. T. Tanabe, M. Notomi, E. Kuramochi, A. Shinya, and H. Taniyama, "Trapping and delaying photons for one nanosecond in an ultrasmall high-Q photonic-crystal nanocavity," Nature Photonics **1**, 49–52 (2006).
9. Y. Tanaka, J. Upham, T. Nagashima, T. Sugiya, T. Asano, and S. Noda, "Dynamic control of the Q factor in a photonic crystal nanocavity," Nature Materials **6**, 862 – 865 (2007).
10. I. Fushman, E. Waks, D. Englund, N. Stoltz, P. Petroff, and J. Vučković, "Ultrafast nonlinear optical tuning of photonic crystal cavities," Appl. Phys. Lett. **90**(9), 091118 (pages 3) (2007).
11. D. Englund, H. Altug, B. Ellis, and J. Vuckovic, "Ultrafast Photonic Crystal Lasers," Laser Photon. Rev. **2**, 1863–8880 (2008).
12. X. Chen, Y.-S. Chen, Y. Zhao, W. Jiang, and R. T. Chen, "Capacitor-embedded 0.54 pJ/bit silicon-slot photonic crystal waveguide modulator," Opt. Lett. **34**(5), 602–604 (2009).
13. A. R. A. Chalcraft, S. Lam, D. O'Brien, T. F. Krauss, M. Sahin, D. Szymanski, D. Sanvitto, R. Oulton, M. S. Skolnick, A. M. Fox, D. M. Whittaker, H.-Y. Liu, and M. Hopkinson, "Mode structure of the L3 photonic crystal cavity," Appl. Phys. Lett. **90**(24), 241117 (pages 3) (2007).
14. D. Englund, D. Fattal, E. Waks, G. Solomon, B. Zhang, T. Nakaoka, Y. Arakawa, Y. Yamamoto, and J. Vučković, "Controlling the Spontaneous Emission Rate of Single Quantum Dots in a Two-Dimensional Photonic Crystal," Phys. Rev. Lett. **95**, 013,904 (2005).
15. M. Fujita, S. Takahashi, Y. Tanaka, T. Asano, and S. Noda, "Simultaneous Inhibition and Redistribution of Spontaneous Light Emission in Photonic Crystals," Science **308**(5726), 1296–1298 (2005).
16. J. Talghader and J. S. Smith, "Thermal dependence of the refractive index of GaAs and AlAs measured using semiconductor multilayer optical cavities," Appl. Phys. Lett. **66**, 335 (1995).

17. F. G. D. Corte, G. Cocorullo, M. Lodice, and I. Rendina, "Spectral dependence of the change in refractive index due to carrier injection in GaAs lasers," Appl. Phys. Lett. **77**, 1614 (2000).
18. S. G. Johnson, M. Ibanescu, M. A. Skorobogatiy, O. Weisberg, J. D. Joannopoulos, and Y. Fink, "Perturbation theory for Maxwell's equations with shifting material boundaries," Phys. Rev. E **65**(066611) (2002).
19. E. D. Palik, *Handbook of Optical Constants of Solids* (Academic Press, San Diego, CA, 1998).
20. J.-K. Hwang, H.-Y. Ryu, D.-S. Song, I.-Y. Han, H.-W. Song, H.-K. Park, Y.-H. Lee, and D.-H. Jang, "Room-temperature triangular-lattice two-dimensional photonic band gap lasers operating at 1.54μm," Appl. Phys. Lett. **76**(21), 2982–2984 (2000).
21. C. Monat, C. Seassal, X. Letartre, P. Viktorovitch, P. Regreny, M. Gendry, P. Rojo-Romeo, G. Hollinger, E. Jalaguier, S. Pocas, and B. Aspar, "InP 2D photonic crystal microlasers on silicon wafer: room temperature operation at 1.55 um," Electron. Lett. **37**(12), 764–766 (7 Jun 2001).
22. G. Vecchi, F. Raineri, I. Sagnes, A. Yacomotti, P. Monnier, T. J. Karle, K.-H. Lee, R. Braive, L. L. Gratiet, S. Guilet, G. Beaudoin, A. Taneau, S. Bouchoule, A. Levenson, and R. Raj, "Continuous-wave operation of photonic band-edge laser near 1.55 um on silicon wafer," Opt. Express **15**(12), 7551–7556 (2007).
23. B. B. Bakir, C. Seassal, X. Letartre, P. Regreny, M. Gendry, P. Viktorovitch, M. Zussy, L. D. Cioccio, and J.-M. Fedeli, "Room-temperature InAs/InP Quantum Dots laser operation based on heterogeneous "2.5 D" Photonic Crystal," Opt. Express **14**(20), 9269–9276 (2006).
24. Q. Xu, S. Manipatruni, B. Schmidt, J. Shakya, and M. Lipson, "12.5 Gbit/s carrier-injection-based silicon micro-ring silicon modulators," Opt. Express **15**(2), 430–436 (2007).
25. Y. Vlasov, W. M. J. Green, and F. Xia, "High-throughput silicon nanophotonic wavelength-insensitive switch for on-chip optical networks," Nat. Photon **2**, 242 – 246 (2008).
26. R. Schmidt, U. Scholz, M. Vitzethum, R. Fix, C. Metzner, P. Kailuweit, D. Reuter, A. Wieck, M. C. Hübner, S. Stufler, A. Zrenner, S. Malzer, and G. H. Döhler, "Fabrication of genuine single-quantum-dot light-emitting diodes," Appl. Phys. Lett. **88**(12), 121115 (pages 3) (2006).
27. S. Fan, P. Villeneuve, J. Joannopoulos, and H. Haus, "Channel drop filters in photonic crystals," Opt. Express **3**(1), 4–11 (1998).
28. E. Chow, A. Grot, L. W. Mirkarimi, M. Sigalas, and G. Girolami, "Ultracompact biochemical sensor built with two-dimensional photoniccrystal microcavity," Opt. Lett. **29**(10), 1093–1095 (2004).
29. M. Lončar, A. Scherer, and Y. Qiu, "Photonic crystal laser sources for chemical detection," Appl. Phys. Lett. **82**(26), 4648–4650 (2003).
30. D. Englund, A. Faraon, B. Zhang, Y. Yamamoto, and J. Vuckovic, "Generation and transfer of single photons on a photonic crystal chip," Opt. Express **15**, 5550–8 (2007).
31. A. Politi, M. J. Cryan, J. G. Rarity, S. Yu, and J. L. O'Brien, "Silica-on-Silicon Waveguide Quantum Circuits," Science **320**(5876), 646–649 (2008).
32. B. R. Bennett, R. A. Soref, and J. A. D. Alamo, "Carrier-Induced Change in Refractive Index of InP, GaAs, and InGaAsP," IEEE J. Quantum Electron. **26**, 113–122 (1990).
33. D. A. B. Miller, C. T. Seaton, M. E. Prise, and S. D. Smith, "Band-Gap¯Resonant Nonlinear Refraction in III-V Semiconductors," Phys. Rev. Lett. **47**(3), 197–200 (1981).
34. D. S. Chemla, I. Bar-Joseph, J. M. Kuo, T. Y. Chang, C. Klingshirn, G. Livescu, and D. A. B. Miller, "Modulation of absorption in field-effect quantum well structures," IEEE J. Quantum Electron. **24**, 16641676 (1988).
35. H. Casey, D. D. Sell, and K. W. Wecht, "Concentration dependence of the absorption coefficient for n– and p–type GaAs between 1.3 and 1.6 eV," J. Appl. Phys. **46**, 250 (1975).
36. T. H. Stievater, X. Li, D. G. Steel, D. Gammon, D. S. Katzer, D. Park, C. Piermarocchi, and L. J. Sham, "Rabi Oscillations of Excitons in Single Quantum Dots," Phys. Rev. Lett. **87**(13), 133,603 (2001).

1. Introduction

A major challenge in the development of future integrated circuits is increasing the bandwidth of interconnects without raising the power consumption. Replacing electrical with optical interconnects could provide a solution at length-scales down to the chip-to-chip and intra-chip level[1, 2, 3]. Planar photonic crystals (PPCs) represent an attractive medium for optical interconnects because they allow wavelength-scale guiding of light, efficient multiplexing, and on-chip integration[4, 5, 6]. Optical modulation in PPCs has been achieved by optically injected carriers[7, 8, 9, 10] and direct modulation of photonic crystal lasers[11]. However, electrically controlled modulation is required for practical devices. Such electrical control was demonstrated recently in a Mach-Zehnder interferometer configuration employing the slow light effect in a photonic crystal waveguide to shrink the active region to $\sim 300~\mu$m [12]. Here we describe a design based on a photonic crystal cavity with a volume of only $\sim 0.8(\lambda/n)^3$, where $n = 3.4$ is the refractive index of GaAs at the wavelength $\lambda = 1.35\mu$m. The optical transmission of
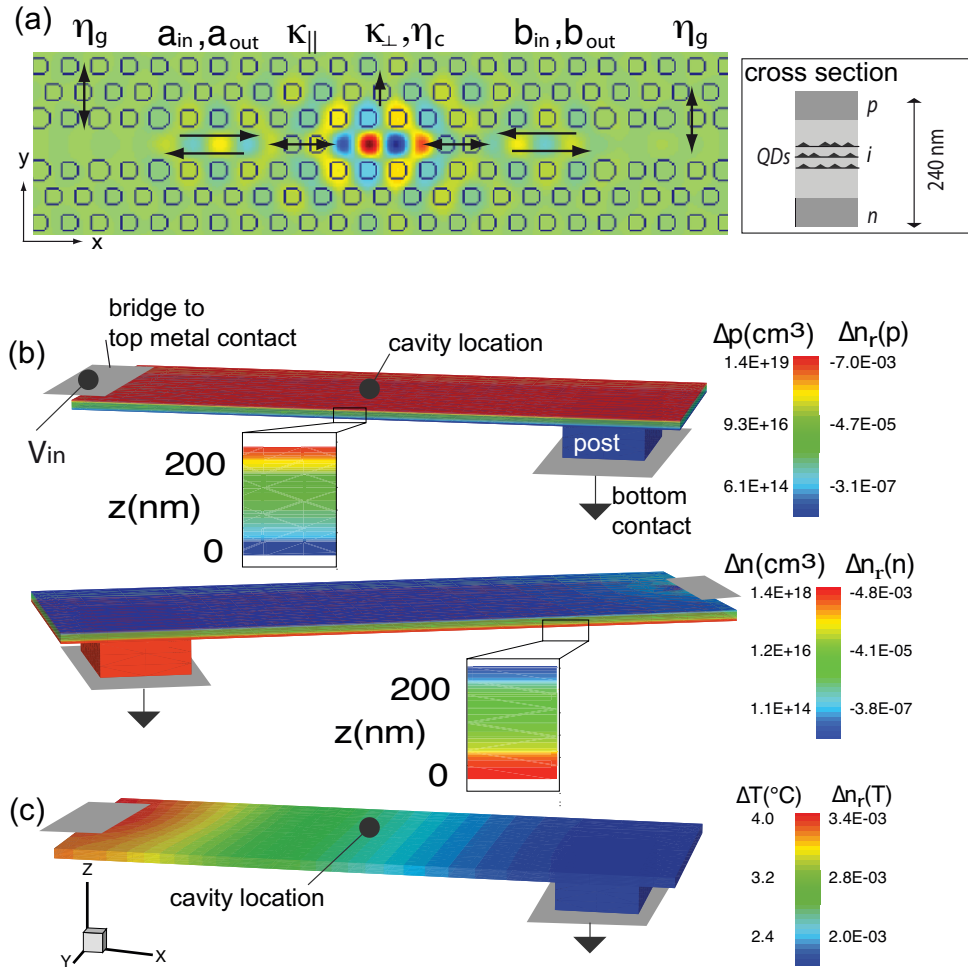
Fig. 1. The photonic crystal circuit. (a) The resonant electromagnetic mode; shown here is the magnetic field component in the z-direction, simulated by FDTD. The cavity energy loss rate is $\kappa_\perp$ and the cavity-waveguide coupling rate $\kappa_\parallel$; the cavity and grating intensity loss are collected with efficiencies η_c, η_g, respectively. (b) Steady-state change in hole density Δp [top] and electron density Δn [bottom], and associated index change $\Delta n_r(p)[\Delta n_r(n)]$, under 3V forward bias. (c) Steady-state change in temperature, ΔT, and associated index change $\Delta n_r(\Delta T)$, under 3V forward bias.

the cavity is shifted by carrier injection, with a measured modulation visibility up to 35%. The nanocavity modulator has the potential to operate with an active region on the wavelength-scale, enabling a very compact design with sub-fF capacitance and large modulation bandwidth.

2. Device design and fabrication

The optical device is shown in Fig.1(a). It consists of a modified three-hole defect photonic crystal cavity which is connected on two sides to waveguides in a straight-coupling configuration. The cavity has a vertical-loss limited quality factor of $Q_0 = 56 \cdot 10^3$, estimated by a finite difference time domain (FDTD) simulation. When the cavity is coupled to the waveguides as shown in Fig.1(a), the simulated quality factor decreases to $Q = 9.9 \cdot 10^3$. The coupling rate of
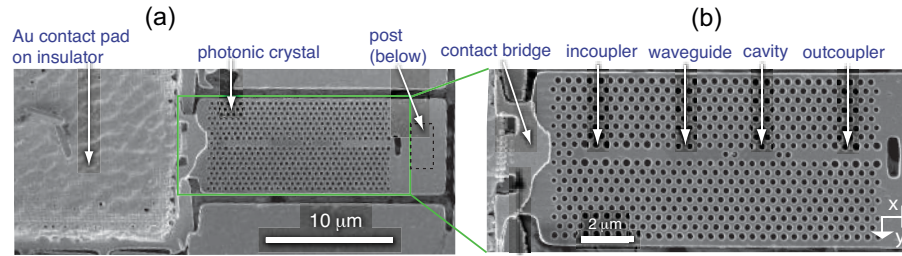
Fig. 2. (a) SEM of the full structure including the contact pad, which connects to the membrane via a bridge across an air trench. The contact pad and bridge are deposited on to of an insulating layer of Poly(methyl methacrylate) (PMMA). (b) Scanning electron micrograph (SEM) of the PPC circuit. The circuit consists of an input grating coupler; input waveguide; cavity; output waveguide; and output grating coupler.

the cavity field into one waveguide, $\kappa_{||}$, relative to the vertical cavity field decay rate $\kappa_{\perp}$ is estimated to be $\kappa_{||}/\kappa_{\perp} \sim 2.3$, where $2\kappa_{||} = \kappa - \kappa_{\perp}$, with $\kappa_{\perp} = \omega/2Q_0$ estimating the vertical-loss limited cavity loss rate and $\kappa = \omega/2Q$. In our design, light is scattered out of the plane from the ends of the waveguides by integrated grating structures consisting of perturbations in the waveguide with a period that matches the excited waveguide mode.

The sample is grown by molecular beam epitaxy (see Appendix A). The photonic crystal membrane is illustrated in Fig. 1(a) and contains a vertical p-i-n diode for carrier injection. Three quantum dot (QD) layers are used for the characterization of the photonic crystal structure as an internal light source. However, the QDs are not required for the modulation of the signal beam and could be omitted in future designs. The photonic crystal structure was fabricated by a combination of electron beam lithography, wet/dry etching, and metal deposition steps for the electrodes and contact bridges (see Appendix B).

Current is injected through a gold bridge that connects to the *p*-layer of the photonic crystal membrane. The bridge, which crosses an insulating air gap in the GaAs top membrane, also serves as structural support, holding up one end of the structure (Fig. 2(a,b)). The other end is supported by an *n*-doped post, which remains after the selective wet etch. The post is connected through the *n*-doped substrate to the sample's bottom metal contact, which is grounded. The signal voltage is applied to the contact pad (Fig. 2(a)). We simulated the electrical properties of the structure using the Sentaurus software package, which gives the electron and hole densities, as well as the temperature, as a function of the applied voltage. Figure 1(b) shows the steady-state change in the hole and electron densities under a forward bias of 3 V.

3. Experiment

The structures are mounted in a confocal microscope setup which allows for independent positioning of two laser beams: a narrow-linewidth continuous-wave (cw) probe beam at a wavelength that is tunable from 1250-1369 nm; and a pump beam for exciting photoluminescence (PL) with a wavelength of 633 nm. A movable pinhole in the image plane of the confocal microscope setup allows collection of light from different regions of the chip with a diameter as small as $\sim 3\mu$m. All measurements are performed at room temperature.
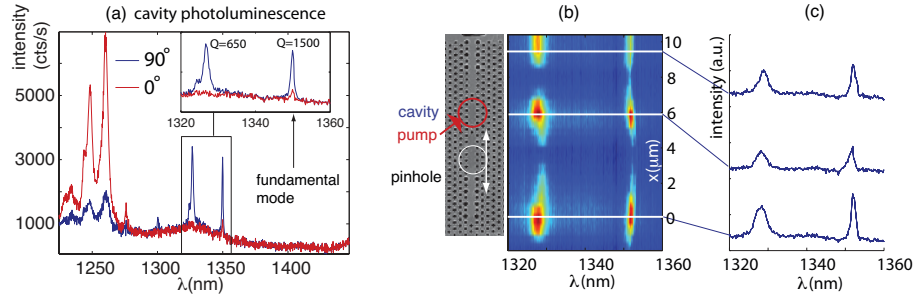
Fig. 3. (a) PL when the cavity is pumped by a focused laser at 633 nm. The fundamental mode is polarized in the $y-$direction (90°). (b) PL when the cavity is pumped and a pinhole in the image plane is scanned across the length of the device. (c) The spectra at the top coupler; the cavity; and the bottom coupler. The intensity through the bottom coupler is slightly larger because the second-order grating has four periods, whereas the top grating only has three. The spectra in (b,c) are acquired using a diffraction grating with lower resolution than in (a).

3.1. Device characterization

We first characterize the photonic circuit by the QD photoluminescence that is excited using the 633 nm pump laser. Figure 3(a) shows the spectrum that is observed when the cavity is optically pumped and the observation pinhole is open to collect from the full structure. We observe two cavity modes at wavelengths $\lambda = 1350$ nm ($Q = 1500$) and $\lambda' = 1327$ nm ($Q' = 650$), both polarized perpendicular to the long cavity axis. We identify these modes as the fundamental and first-order modes of the L3 cavity, which are both expected to be orthogonally polarized to the other higher-frequency modes near 1250 nm in Fig. 3[13]. The observed Q factor of the fundamental mode is lower than the simulated value of $9.9 \cdot 10^3$, which we attribute to fabrication imperfections that lead to a larger vertical cavity loss rate $\kappa_\perp$ (see Appendix D). We will from now on concentrate on the fundamental cavity mode at $\lambda \approx 1350$ nm. To characterize the transfer of the cavity emission to the waveguide and grating couplers, we graph in Fig.3(b,c) the PL collected when the cavity is pumped while the pinhole is scanned across the length of the device. The QD PL collected through the waveguides accounts for $\sim 85\%$ of the total collected emission.

Next, we use the electroluminescence (EL) from the QDs in the p-i-n diode to characterize the electrical pumping of the structure. Figure 4(a) plots the EL when the pinhole is closed around the outcoupling grating. The voltage is pulsed at 1 kHz with a 1% duty cycle to reduce heating. We observe both the fundamental and first-order mode at a voltage above 3 V, which corresponds to a current of 18 μA (see Fig. 4(c)). The resonances are blurred because of fluctuations of free carriers and temperature during the pump cycles; as a result, the high-Q fundamental mode appears lower than the the first-order mode, although their relative areas are roughly the same as under in the PL in Fig. 3(a). From simulations, we estimate that the carriers distribute rather evenly across the whole membrane, as seen in Fig. 1(b). The cavity modes are visible above the background EL because the cavity-coupled QDs emit more rapidly through the Purcell effect and because of higher out-coupling compared to the unpatterned material[14, 15]. Above a voltage of 4 V, the EL drops rapidly because of heating of the membrane.

We will now use the EL spectra to estimate the cavity index change due to carriers, $\Delta n_r(n, p)$, and temperature, $\Delta n_r(T)$:

$$\Delta n_r = \Delta n_r(n, p) + \Delta n_r(T), \qquad (1)$$

where n and p are the electron and hole concentrations, respectively, and T is the temperature. For the carrier-dependent term, we consider contributions due to bandgap narrowing
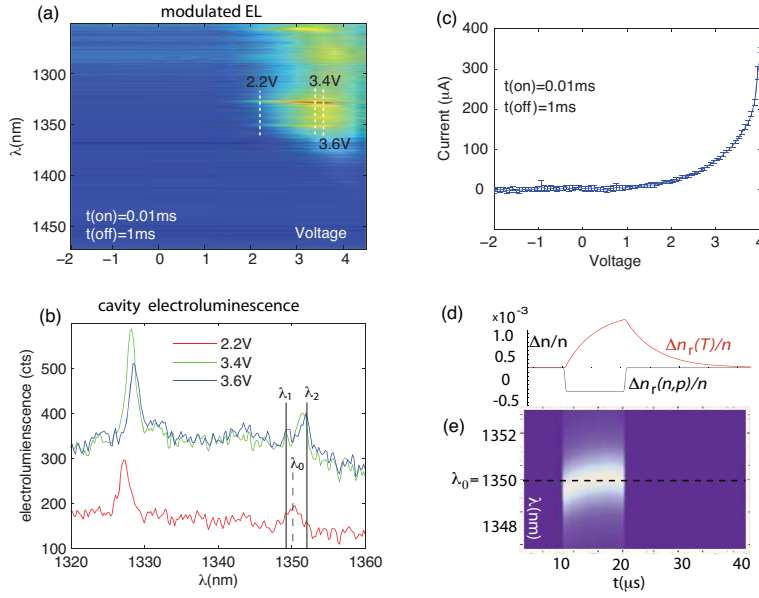
Fig. 4. (a) Electroluminescence spectrum as the pulsed bias voltage is swept from -2 to 4.5V. (b) The EL spectra corresponding to the dashed lines in (a) show that the cavity resonance splits into two discernable peaks at higher voltage. (c) Measured current under pulsed excitation. (d) When a $10\mu s$ square-wave voltage with amplitude 3V is applied across the cavity, the cavity refractive index shifts by both free carrier injection and temperature change, which are estimated in this plot. (e) Expected electroluminescence when the cavity is pumped with the same $10\mu s$ long square-wave. The cavity first rapidly blue-shifts away from the cold-cavity resonance λ_0 due to free carrier injection, and then red-shifts over a longer time scale $\sim 5\mu s$ due to heating.

$(\Delta n_r(n,p)_{BG})$, bandgap filling $(\Delta n_r(n,p)_{BF})$, and free carrier effects $(\Delta n_r(n,p)_{FC})$. As derived in Appendix C, the latter two contributions are dominant, and we approximate their combined effect on n_r as

$$\begin{aligned} \Delta n_r(n,p) &\approx \Delta n_r(n,p)_{BF} + \Delta n_r(n,p)_{FC} \\ &= -5.4\cdot 10^{-21}(\Delta n\cdot\mathrm{cm}^3) - 2.5\cdot 10^{-21}(\Delta p\cdot\mathrm{cm}^3) \end{aligned} \qquad (2)$$

The temperature-dependent index change is modeled as

$$\Delta n_r(T) = 8.4\cdot 10^{-4}\Delta T, \qquad (3)$$

where ΔT is the temperature change from 300 K[16, 17].

Experimentally, we can deduce the dielectric index change Δn from the frequency shift $\Delta\omega_c$ in the cavity resonance, using second order perturbation theory [18]

$$\Delta\omega_c \approx -\frac{\omega_c}{2}\frac{\int \Delta\varepsilon\|\vec{E}\|^2}{\int \varepsilon\|\vec{E}\|^2} \qquad (4)$$

From FDTD simulations, we note that the cavity field is primarily in the high-index material. We can then approximate, for a small index shift Δn, that

$$\frac{\Delta\lambda_c}{\lambda_c} \approx \frac{\Delta n}{n_0}, \qquad (5)$$
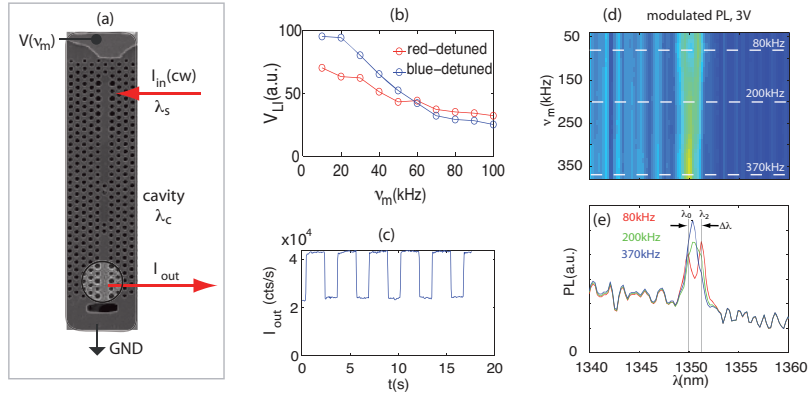
Fig. 5. (a) Setup for cavity transmission experiment. The laser at wavelength λ_s is coupled into the input grating; through the cavity; and out-coupled through through the bottom grating, which is selected with a pinhole. (b) The signal is modulated at v_m and measured using lock-in detection, yielding the demodulate signal voltage V_{LI}. We measured V_{LI} for λ_s red-detuned and blue-detuned from the zero-voltage cavity frequency. (c) Cavity transmission measured in time on a spectrometer. (c) PL collected from cavity as function of the frequency of electrical control pulses at a forward bias of 3V. (d) PL under electrical injection at 80kHz; 200kHz; and 370kHz.

where $n_0 = 3.4$ is the index of GaAs at a wavelength of 1.3 μm [19]. Eqs. [2,3] show that temperature and carrier-mediated shifts on the cavity resonance are expected to be competing effects.

Figure 4(b) plots the EL spectra at the voltages indicated in Fig. 4(a). As the voltage is increased from 2.2V to above 3V, the cavity resonance separates from λ_0 into two peaks centered at λ_1, λ_2, which are split by 2.2 nm (the splitting is not visible for the higher order mode at 1327 nm because of its lower Q). λ_1 appears slightly blue-detuned from λ_0, which would indicate index modulation by free-carriers and/or band-filling. The carrier-induced blue shift is expected to occur rapidly since the electrical response of the structure is expected to be limited by a short RC-response time of only $\tau_{RC} \sim 3$ ns, as described later. The red-shift to λ_2 occurs through heating of the structure on the time scale of $\sim 5\mu$s (estimated from measurements with varied electrical pulse length). From the red shift, we calculate a temperature-induced refractive index shift of $\Delta n_r(T) \approx 1.3 \cdot 10^{-3}$ and a corresponding $\Delta T \approx 1.56°$C. The blue-shift indicates $\Delta n_r(n, p) \approx -1 \cdot 10^{-3}$.

We compare these experimentally obtained index variations to numerical simulations. From the carrier simulations in Fig. 1(b), we estimate that at the location of the cavity and at $V_{in} = 3$ V, $\Delta n_r(n, p) \approx -2 \cdot 10^{-3}$, averaged over the membrane thickness, which is fairly close to our observation. The temperature simulation predicts $\Delta n_r(T) \approx 2.2 \cdot 10^{-3}$, which is also reasonably close to our observation. A time-dependent simulation of the carrier and temperature index shifts gives the cavity evolution after the control pulse is turned on (Fig. 3(d)). This simulation indicates that the cavity resonance first rapidly shifts to short wavelengths due to the carrier-induced refractive index change, and then shifts to longer wavelength because of heating.

3.2. Optical modulation through the photonic crystal cavity

The electrical control of the cavity resonance frequency allows the modulation of an incident narrow-band laser field. As illustrated in Fig. 5(a), an external laser is coupled through the input grating into the waveguide. If it is on resonance with the cavity frequency, it is transmitted to the output waveguide and scattered by the grating towards the objective lens. If it is off-resonance, it

is reflected by the cavity. The coupling efficiency into the grating couplers is low – we estimate about 1-2%. To reduce light that does not couple into the waveguides, we observe the transmission in the crossed polarization: the input beam is polarized at $45°$ to the waveguide, while the output is observed at $-45°$. To further reduce background, the output is also spatially filtered using the pinhole to select the output grating. Figure 5(c) shows the transmission I_{out} observed on the spectrometer when the signal beam's wavelength $\lambda_s = 1351$ nm, which is red-detuned by 1 nm from the cavity frequency at zero bias field, and is close to the red-detuned peak at λ_2 in Fig. 4(b). The visibility is estimated at $(max(I_{out}) - min(I_{out}))/(max(I_{out}) + min(I_{out})) \sim 0.35$. This value is lower than the expected value of ~ 0.7 for the cavity transmission at a detuning of 1nm, largely due to background from scattering on the sample. We also measured the transmission when the laser was blue-detuned by ~ 0.5 nm from the zero-bias cavity wavelength, close to the peak λ_1 in Fig. 4(b). Because the transmitted signal intensity was small ($\sim 1 \mu W$) due to low coupling through the input grating, it was necessary to measure the transmitted amplitude using a lock-in amplifier, which limited the modulation frequency measurement to the lock-in amplifier's cut-off frequency of 100 kHz. Figure 5(b) shows lock-in amplitude V_{LI}. The lock-in signal and hence the modulation amplitude drops off near 40 kHz. This slow modulation bandwidth can only be attributed to the slow thermal fluctuation of the cavity. Beyond this modulation frequency, the cavity should thermally stabilize at some offset from the 'cold-cavity' resonance. Unfortunately, because of limited stability in the optical alignment and the low bandwidth of the lock-in amplifier, it was not possible to accurately measure the high-frequency modulation after adjusting for the thermal offset of the cavity; we plan to study this in future work. We note that the thermal stability could be greatly improved in future experiments by placing the cavities on top of a low-index substrate such as sapphire or silicon dioxide for improved thermal conductivity[20, 21, 22, 23].

We can further study the modulation of the cavity by considering the photoluminescence of the cavity while additional carriers are electrically injected. Figures 4(b,c) plot the photoluminescence when the cavity is excited with the 633 nm pump laser and the structure is electrically modulated with a $0 - 3$V square wave at a modulation rate ν_m and duty cycle of 20%. The integration time is 100 ms — much longer than the switching time. At low frequency, we observe a cavity splitting of $\Delta\lambda_c \approx 1.30$ nm, which indicates a refractive index change of the cavity $\Delta n/n \approx 9.6 \cdot 10^{-4}$. The splitting blurs at a driving frequency from $\nu_m \sim 150$ to ~ 300 kHz; we speculate that this occurs because the cavity does not reach steady-state temperature during each pump period. Above 300 kHz, the blurred feature narrows into a single peak that is red-shifted by a constant $\Delta\lambda = 0.4$ nm from λ_0. At this range of modulation frequencies, the temperature fluctuations decrease as the modulation is faster than the thermal response time, and the cavity remains at a constant temperature-induced offset.

At present, the modulation speed of the device is much slower than optically modulated photonic crystal structures [7, 8, 9, 10]. Since the cavity size and quality factor of the present device is similar to that of the isolated cavities reported in [10], we expect it to have similar switching speed exceeding 10 GHz with optical excitation. On the other hand, electrically controlled modulators based on photonic crystal waveguides[12] and microdisks [24, 25] have been demonstrated in recent years, with modulation speeds now reaching or exceeding 10 GHz. The rapid progress in these architectures suggests that high-speed electrical control in photonic crystal cavities will be possible as well. Indeed, the much smaller size of the PC-cavity network enables significantly lower capacitance, which could increase speed and reduce the power consumption. The thermal stabilization seen in the PL under modulation exceeding 200 kHz suggests operating beyond this frequency with a faster detection technique. To estimate the ultimate modulation speed, we measured the RC time constant. The capacitance was directly

measured to be only 3 pF[1], while the resistance was estimated at 1.1 kΩ from the forward bias part of the I-V curve, yielding an RC time constant of $\sim$ 3ns.

4. Conclusions

In conclusion, we have demonstrated a compact, electrically controlled modulator based on a photonic crystal nanocavity. The small size and capacitance promises operation at high bandwidth with low power consumption, while enabling a high degree of integration on a chip. While we measured $1/RC \sim 300$ MHz, the modulation speed in future designs could be increased significantly by changing the refractive index only in the photonic crystal cavity whose area is less than 100 times the area of the full membrane in this study. Lateral dopant implantation could allow a small junction with sub-fF capacitance and a time constant of $RC < 10$ ps[26]. The frequency-selective modulation of the cavity is suited for wavelength division multiplexing, which greatly increases the total interconnect bandwidth and may become essential in off-chip optical interconnects[1]. Because the cavity modulator relies on a resonance shift rather than absorption, it is expected that it can operate at high optical intensity. We note that operation in the present reflective configuration may require optical isolation in some systems. Alternatively, the light could be transmitted into another waveguide in a channel drop filter design[8, 27]. Besides optical interconnects, electrically controlled photonic crystal networks have promise in applications including biochemical sensing [28, 29] and quantum information processing in on-chip photonic networks [30, 31].

A. Sample growth

The sample is grown by molecular beam epitaxy on an *n*-type GaAs substrate. As listed in Table A, it consists of a 1 μm *n*-doped $Al_{0.8}Ga_{0.2}As$ sacrificial layer, a 40 nm *n*-doped GaAs layer, a 160nm intrinsic GaAs membrane that contains three layers of InAs quantum dots (QDs) separated by 50 nm GaAs spacers, a 25 nm *p*-doped GaAs layer and a 15 nm highly *p*-doped GaAs layer to ensure low-resistance contacts. The QD layers were grown by depositing 2.8 monolayers (ML) of InAs at 510°C at a growth rate of 0.05 ML/s. To achieve emission at $\sim$ 1.3 μm, the dots were capped with a 6 nm $In_{0.15}Ga_{0.85}As$ strain-relaxing layer.

Table 1. Membrane

layer	dopant	doping	thickness
p+	C-doped	2×10^{19}cm^{-3}	15nm
p	C-doped	2×10^{18}cm^{-3}	25nm
intrinsic with three layers of InAs QDs (density of 300 QDs/μm^2)	-	-	160nm
n	Si-doped	2×10^{18}cm^{-3}	40nm
Al0.8Ga0.2As sacrificial layer/pillar	Si-doped	2×10^{18}cm^{-3}	1μm

B. Fabrication

First, metal contacts are deposited on the n-type substrate and annealed to form the bottom contacts. These contacts consist of Au/Ge/Ni/Au layers. Then the photonic crystal structure, isolating gaps, and trenches are defined in a Poly(methyl methacrylate) (PMMA) mask by electron beam lithography (EBL) and dry etching. The top contact mask is created by a EBL exposure in

---

[1]The capitance was measured with a Hewlett-Packard 4275A multi-frequency LCR meter.

a PMMA layer. The bridge structure is created in the same step by over-exposure of the PMMA resist over an isolation gap, which leaves a hard cross-linked polymer after development of the resist. The second EBL exposure thus creates metal-on-semiconductor and metal-on-polymer in one step. The p-contact consists of Pt/Ti/Pt/Au layers. After the metallization, the free-standing membrane is created by removing the sacrificial AlGaAs layer using a hydrofluoric acid-based selective wet etch. This etch is timed to leave behind the post to the bottom contact.

C.   Index dependence on carriers and temperature

The primary sources of refractive index change in the GaAs membrane are bandgap narrowing, bandgap filling, free carrier effects, and temperature effects. We neglect band-gap narrowing as it only changes slowly with carrier density at high carrier densities and is far weaker than band-filling effects at 1350 nm[32]. Because the carrier effects are independent, we can express Δn_r as the sum due to band filling, free carrier effects, and thermal changes, respectively:

$$\Delta n(n, p, T) = \Delta n(n, p)_{BF} + \Delta n(n, p)_{FC} + \Delta n(T) \tag{6}$$

We follow the discussion in Ref.[32] to estimate the carrier contributions $\Delta n(n, p)_{BF} + \Delta n(n, p)_{FC}$. Using fundamental constants[32], a DC refractive index $n_g = 3.6$, normalized electron and hole masses $m_e = 0.066$, $m_h = 0.45$, and assuming equal Δn and Δp,

$$\Delta n_r(n, p)_{BF} \approx -2 \times 10^{-21} (\Delta n + \Delta p) \tag{7}$$

$$\Delta n_r(n, p)_{FC} = -\frac{e^2 \lambda^2}{8\pi^2 c^2 \varepsilon_0 n_0} \left(\frac{\Delta n}{m_e} + \frac{\Delta p}{m_h} \right) \tag{8}$$

$$\simeq -3.4 \times 10^{-21} \Delta n - 5.0 \times 10^{-22} \Delta p \tag{9}$$

We note also that larger refractive index changes are possible if working with photon energies nearer to the band edge [33] or by exploiting the index change in quantum confined structures [34]. The temperature dependence of the refractive index follows

$$\Delta n_r(T) = n_0 \cdot \alpha (T - T_0), \tag{10}$$

where T_0=300K is the initial temperature and T is the operating temperature.

We chose n_r=3.410 for GaAs at $\lambda = 1.3\mu$m T=300°C, after [19]. α is the thermo-optic constant, which we take to be 2.5×10^{-4}/°C as an interpolation between Refs.[16, 17] for $\lambda = 1.35\mu$m.

Therefore, the total expected change in refractive index is

$$\Delta n_r(n, p, T) = -5.4 \times 10^{-21} \Delta n - 2.5 \times 10^{-21} \Delta p + 8.5 \times 10^{-4} \Delta T \tag{11}$$

D.   Photonic circuit model and characterization

Referring to Fig.1, we represent the field amplitudes of the forward and backward propagating modes in the left-hand waveguide as a_{in}, a_{out}; the field in the cavity mode as c; and the amplitudes in the right-hand waveguide as b_{in}, b_{out}. The cavity field is coupled to the waveguides by the in-plane energy coupling rate $\kappa_{\parallel}$ and experiences field loss at the rate $\kappa_{\perp}$ vertically. From coupled mode theory[4], we have

$$\frac{dc}{dt} = -i\omega_c c - 2\kappa_{\parallel} c - \kappa_{\perp} c + \sqrt{2\kappa_{\parallel}} (a_{in} + b_{in}) + p(t) \tag{12}$$

$$a_{out} = -a_{in} + \sqrt{2\kappa_{\parallel}} c \tag{13}$$

$$b_{out} \quad = \quad -b_{in} + \sqrt{2\kappa_{||}}c \qquad (14)$$

$$(15)$$

To describe the pumping of the QDs in the cavity and the observation of PL through the cavities and the waveguides, we solve this set of equations on resonance ($\omega = \omega_c$). We assume that the intensity collection efficiency is η_g from the gratings and η_c from the cavity. Then the steady-state solution to Eqs.12 yields the fraction of the cavity intensity that occurs through both gratings, $\eta_{g,c} = 1/(1+x)$, where $x = \eta_c\kappa_{\perp}/4\eta_g\kappa_{||}$.

Assuming that the total loss rate in the waveguides is much lower than the loss through coupling to the gratings and cavity, as supported below, we can estimate from the measured intensities in Fig. 3(c) that $\eta_{g,c} \approx 0.85$. Assuming $\kappa'_{\perp}/\kappa_{||} \sim 17$, where $\kappa'_{\perp}$ is the cavity loss rate estimate from experiment and $\kappa_{||}$ is derived from the simulation, we estimate $\eta_c/\eta_g \sim 0.04$.

To model the transmission, we set $p(t) = 0$ in Eqs. (12) and solve for the transmission

$$T(\omega) = \frac{|b_{out}|^2}{|b_{in}|^2} = |1 + (\kappa_{\perp} - i\Delta)/2\kappa_{||}|^{-2}, \qquad (16)$$

where $\Delta = \omega - \omega_c$.

We estimated the absorption in the semiconductor due to the doping layers and quantum dots. First, we consider only the doping regions. The absorption in the p+ layer results in an absorption coefficient $|\psi|^2\alpha$, where $|\psi|^2 \sim 5 \cdot 10^{-3}$ approximates the mode intensity overlap and $\alpha \sim 100/$cm represents the bulk absorption coefficient of the doped layer at room temperature[35]. By comparison, the absorption coefficient in the n-type layer more than one hundred times smaller[35]. Therefore we have the doping-layer absorption $\alpha_d \sim 0.5/$cm, dominated by the p+ layer. The absorption in the quantum dots is more difficult to estimate. Using the exciton absorption coefficient reported in Ref.[36] for three layers of QDs with number density of $300/\mu$m^2, and considering a measured inhomogeneous distribution of the exciton resonances of ~ 50 nm, gives $\alpha_{QD} \sim 2/$cm.

We can relate the absorption coefficient to a 'material-limited Q_M' in the cavity. The expected total Q_{tot} value is then related to the scattering-limited Q, which we calculated by FDTD, and the material Q_M, by $Q_{tot}^{-1} = Q_M^{-1} + Q^{-1}$. Q_M is derived by noting that the 'distance traveled' in the material-limited cavity during the cavity decay time, τ, is $\tau c/n = 1/\alpha$. From $\tau = \omega/Q_M$, we then obtain $Q_{M,d} \sim 300 \cdot 10^3$ for the doping layers, and $Q_{M,QD} \sim 80 \cdot 10^3$ for the QDs. Since the losses due to the QDs are significant, the QDs should be omitted or their number density greatly reduced in future designs. However, we note that the material losses due to the contacts themselves are negligible compared to the scattering losses in the cavity.